

Chapter 1

Nano-scale testing of nanowires and carbon nanotubes using a microelectromechanical system

Horacio D. Espinosa*, Yong Zhu[†], Bei Peng and Owen Loh
*Department of Mechanical Engineering, Northwestern University
2145 Sheridan Road, Evanston, IL USA 60208,
espinosa@northwestern.edu*

The need to characterize nanometer-scale materials and structures has grown tremendously in the past decade. These structures may behave very differently from their larger counterparts and must be carefully characterized before their full potential is realized. The challenging task of mechanical characterization requires an entirely new set of techniques to achieve the force and displacement resolution needed to accurately characterize these structures. This chapter begins with a brief review of some of the methods used in mechanical characterization of nano-scale specimens, followed by a detailed description of a MEMS-based material testing system. This MEMS-based system allows for continuous observation of specimen deformation and failure with sub-nanometer resolution by scanning or transmission electron microscope while simultaneously measuring the applied load electronically with nano-Newton resolution. Special emphasis is placed on modeling and analysis of a thermal actuator used to apply a displacement-controlled load to the tensile specimen as well as the electrostatic load sensor. Finally, experimental results demonstrating the advantages of the MEMS-based system are presented.

1.1. Introduction

The emergence of numerous nano-scale materials and structures within the past decade has prompted a need for methods to characterize their

*Corresponding author

[†]Currently at University of Texas at Austin
Center for Mechanics of Solids, Structures and Materials
210 East 24th Street
Austin, TX 78712

unique mechanical properties. For example, nanotubes and nanowires are seen as ideal structures for use in a variety of applications ranging from nanocomposites to nanoelectromechanical systems. However, their scale presents a new set of challenges to the mechanics community. Identification of their properties and deformation mechanisms requires techniques of loading, measuring, and imaging with finer resolutions than previously achieved. As a result, these structures demand quantitative *in situ* mechanical testing by scanning or transmission electron microscope, or scanning probe microscope.

1.2. Mechanical characterization techniques

The precision required in nano-scale material testing is prohibitive to many techniques used previously on larger scales. This is due to strict requirements in: handling, manipulating, and positioning specimens; applying and measuring forces in the nano-Newton range, and; measuring local deformation. Existing material testing techniques intended to overcome these limitations can be roughly categorized into three types: (1) dynamic vibration, (2) bending, and (3) tensile tests.

1.2.1. *Dynamic vibration*

The Young's modulus of nanostructures can be estimated by observing their vibrations. Treacy *et al.*¹ determined the Young's modulus of multi-walled carbon nanotubes (MWNTs) by measuring the amplitude of their thermal vibrations within a transmission electron microscope (TEM). One end of the MWNT was attached to the edge of a nickel ring while the other end remained free. The ring and MWNT were then imaged in the TEM. The frequency of the thermal vibration of the MWNT was significantly faster than the integration time required for imaging, causing the free end to appear blurred. The authors used the blurred region to determine an envelope of vibration. This envelope increased significantly with temperature, indicating it was indeed a thermal vibration. The Young's modulus of the MWNT was estimated based on the size of the envelope.

Poncharal *et al.*² measured the Young's modulus of MWNTs by inducing resonance within a TEM. Here the MWNTs were attached to a gold wire and an electrode was introduced using a piezo-driven translation stage on the TEM holder. An AC voltage was then applied across the wire and electrode, causing oscillatory deflection of the MWNTs toward the elec-

trode. By increasing the driving frequency to the point of resonance, the authors were able to estimate the Young's modulus based on the measured geometry of the MWNTs and their resonance frequency.

1.2.2. *Bending*

Bending techniques, including force spectroscopy atomic force microscopy (AFM),³ nanoindentation,⁴ and on-chip testing,^{5,6} involve application of a known bending force while measuring the resulting displacement. These techniques typically lack the ability to image the specimen during loading. Wong *et al.*⁷ measured the Young's modulus, strength, and toughness of MWNTs and SiC nanorods using an atomic force microscope (AFM). The nanostructures were randomly dispersed on a flat substrate and pinned in place by microfabricated patches. The AFM was then used to bend the cantilevered structures transversely. By measuring the lateral force applied to the AFM probe by the nanostructure, the authors were able to obtain force versus deflection data at various locations along the length of the structure.

In the above method, adhesion and friction between the nanostructure and substrate could not be avoided. To avoid these issues, Walters *et al.*⁸ suspended MWNTs over a microfabricated trench before bending them laterally with an AFM. Salvetat *et al.*⁹ dispersed MWNTs over an alumina ultrafiltration membrane with 200 nm pores. This created similarly suspended nanostructures. The natural adhesion between the MWNTs and membrane was found to be sufficiently strong to fix the MWNTs during testing. The authors then deflected the suspended MWNTs vertically using an AFM probe in contact mode to obtain similar force-displacement measurements.

1.2.3. *Tensile tests*

The tensile test is perhaps the most direct method of determining the Young's modulus of a material. Some tensile techniques allow for simultaneous load measurement and local imaging by AFM,¹⁰ optical interferometry,¹¹ or scanning electron microscopy (SEM).^{12,13} On a larger scale, Pan *et al.*¹⁴ used a stress-strain rig to load a long (approximately 2 mm) MWNT rope in tension. This rope contained tens of thousands of parallel nanotubes. Sharpe *et al.*¹¹ loaded thin films in tension while simultaneously measuring displacement using either a capacitance-based displacement probe or laser interferometry, depending on the size of the sample. To

use laser interferometry, two closely-spaced reflective gauge markers were patterned on the specimen. When shining a laser on these markers, interference fringes form which move as the spacing between the markers changes. These techniques tend to be better suited to the micrometer scale and not to the study of nanostructures such as nanotubes or nanowires due to their limited resolution.

On a smaller scale, Yu *et al.*¹² and Ding *et al.*¹³ used a micro- or nanomanipulator to conduct in situ SEM tensile testing of MWNTs. The authors fixed a single nanotube between two AFM probes by localized electron beam-induced deposition (EBID) of carbonaceous material within the SEM chamber. One of the AFM probes was of low stiffness (less than 0.1 N/m) and used as a load sensor. The other probe was rigid and used to apply tensile load. When the rigid probe was actuated, the soft probe deflected in response to the applied load. The force applied to the nanotube was estimated based on the deflection of the soft cantilever and its known stiffness. The deformation of the nanotube was recorded by the SEM. The Young's modulus and failure strength of the nanotubes were then calculated based on the applied forces and corresponding measured displacements.

Marszalek *et al.*³ attached a gold nanowire to an AFM probe of known stiffness. By lifting the probe a prescribed amount using the piezoelectric actuators of the AFM and observing the corresponding deflection of the probe, they were able to deduce the force applied to the nanowire and corresponding displacement.

Other techniques combine microfabricated and larger-scale devices. These allow alternating SEM or TEM imaging and load or deformation measurement modes through switching of the imaging electron beam between the specimen and microfabricated beams used as load sensors.^{15,16} During this switching, important local deformation events may go unobserved. Finally, some techniques have been developed to provide real time images of the specimen during loading. However, quantitative measurement of load and deformation are not provided simultaneously.^{17,18}

The methods described above represent some of the significant progress made recently in the mechanical testing of nanostructures. However, lack of control in experimental conditions or limited accuracy of force and displacement measurements can limit their applicability. Recent advances in microelectromechanical systems (MEMS) create the potential for material testing systems that overcome some of the described limitations.

1.3. A MEMS-based material testing stage

MEMS lend themselves naturally to material testing at the nanometer scale. These systems consist of combinations of micromachined elements, including strain sensors and actuators, integrated on a single chip. Due to their intermediate size, MEMS serve as an excellent interface between the macro and nano world. Their extremely fine force and displacement resolution allows accurate measurement and transduction of forces and displacements relevant at the nanometer scale. At the same time, the larger feature sizes and signal levels of MEMS allow handling and addressing by macro-scale tools. Furthermore, many of the sensing and actuation schemes employed in MEMS scale favorably. For example, the time response, sensitivity, and power consumption of electrostatic displacement sensors improves as their dimensions shrink.

Electrostatic comb-drive actuators are often used in MEMS-based testing systems to apply time-dependent forces. van Arsdell and Brown¹⁹ repeatedly stressed a micrometer-scale specimen in bending using a comb-drive actuator fixed to one end of the specimen. This comb-drive actuator swept in an arc-like motion while the opposite end of the specimen was fixed, causing bending stresses in the specimen. The comb-drive was also used to measure displacement, allowing for fracture and fatigue data to be collected when testing to the point of failure. Kahn, *et al.*^{20,21} determined fracture toughness by controlling crack propagation in a notched specimen using a comb-drive. One end of the specimen was fixed while the other was attached to a perpendicularly oriented comb-drive.

Electrothermal actuation schemes have also been used to apply loading.^{22,23} In these actuators, Joule heating induces localized thermal expansion of regions of the actuators and an overall displacement. The resulting strains are often measured using an integrated capacitive sensor and may be verified through digital image correlation.

This section presents a detailed description of the design and modeling of a MEMS-based material testing system²⁴ for in-situ electron microscopy mechanical testing of nanostructures. This device allows for continuous observation of specimen deformation and failure with sub-nanometer resolution by SEM or TEM while simultaneously measuring the applied load electronically with nano-Newton resolution. To begin, an analytical model of the thermal actuator used to apply tensile loading includes an electrothermal analysis to determine the temperature distribution in the actuator, followed by a thermomechanical analysis to determine the resulting displace-

ment. A coupled-field finite element analysis complements the analytical model. Next, the differential capacitive sensor is analyzed to determine the applied load from the measured electric signals. Finally, a set of design criteria are established based on the analyses as guidelines for design of similar devices.

1.3.1. Device description

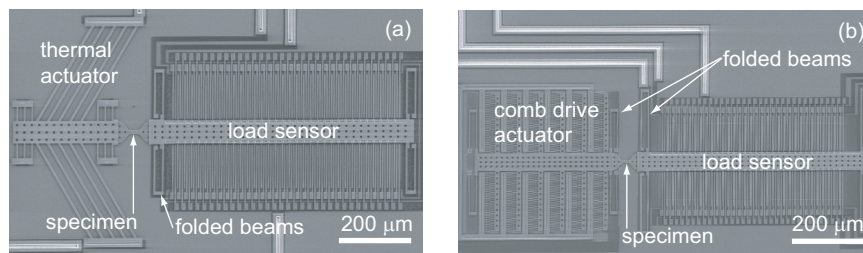


Fig. 1.1. Two variations of the MEMS-based material testing stage. (a) “Displacement controlled” device using a thermal actuator and differential capacitive load sensor. (b) “Force controlled” device using an electrostatic comb-drive actuator and differential capacitive load sensor.

The MEMS-based tensile loading stage^{24–26} consists of a linear actuator and a load sensor with a specimen fixed between them. The actuator is used to apply a tensile load to a specimen attached between the actuator and load sensor, while the load sensor detects the corresponding load. Fig. 1.1a shows the entire device. The electrothermal actuator acts as a “displacement control” in the sense that it applies a prescribed displacement to the specimen regardless of the force required to achieve this displacement (within the functional range of the device). The load sensor is suspended on a set of folded beams of known stiffness and measures the corresponding tensile force applied to the specimen. Fig. 1.1b shows an alternative loading stage using an electrostatic rather than a thermal actuator. The electrostatic actuators works as a “force control”, applying a prescribed force regardless of the resulting displacement (again within a functional range).

While both the thermal and electrostatic actuators lend themselves nicely to standard microfabrication techniques, the remainder of this chapter focuses on the device using the thermal actuator as a case study in the design and modeling involved in building such a device. Electrostatic

actuators have been thoroughly described elsewhere, for example.^{5,27,28}

1.3.2. *Electrothermal actuator*

Electrothermal actuation compliments electrostatic schemes as a compact, stable, high-force actuation technique.²⁹ It involves coupling of electric, thermal, and structural fields. Typically a resistive heating element is used as a heat input. This invokes thermal expansion of the device, resulting in a displacement. As mentioned above, these actuators are considered a “displacement control” as they displace a specific amount for a given heat input (within the limits of buckling and material stiffness).

Various forms of thermal actuators have been employed in systems ranging from linear and rotary microengines,³⁰ to two-dimensional nano-scale positioners,³¹ optical benches,³² and instrumentation for material characterization.³³ By incorporating compliant mechanisms, larger displacements can be achieved.³¹

Modeling of thermal actuators generally takes one of two approaches:

- (1) A sequential electro-thermal and thermo-structural analysis,^{34–36} or;
- (2) A complete coupled three-dimensional finite element analysis (FEA).³⁷

Additional analyses include characterization of the temperature-dependent electro-thermal properties^{29,37} of these devices.

Sections 1.3.3 and 1.3.4 present an analysis of the thermal actuator employed by Zhu and Espinosa^{24,25} in the MEMS-based material testing system. The description begins with derivation of a set of analytical expressions for the response of the thermal actuator using a structural mechanics approach. This analysis is followed by a three-dimensional finite element multiphysics simulation to assess the temperature distribution within the actuator.

1.3.3. *Analytical modeling of the thermal actuator*

A schematic of the thermal actuator to be analyzed is shown in Fig. 1.2. The thermal actuator consists of a series of inclined polysilicon beams supporting a free-standing shuttle. One end of each of the inclined beams is anchored to the substrate while the opposite end connects to the shuttle. Thermal expansion of the inclined beams, induced by Joule heating, causes the shuttle to move forward. This heating is the result of current flowing through the beams driven by a voltage applied across the two anchor

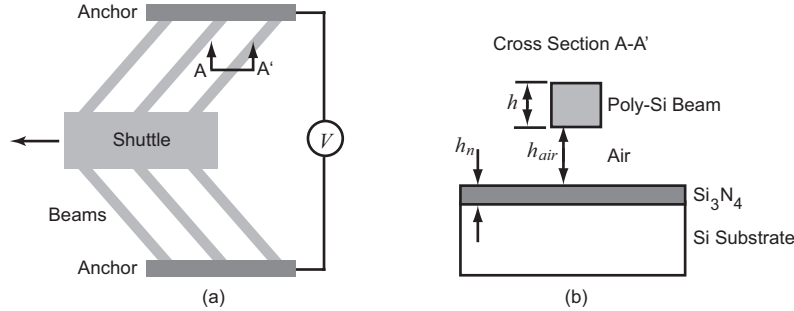


Fig. 1.2. (a) Schematic of the thermal actuator. (b) Cross section of a single beam suspended over the substrate.

points.³⁸ Modeling of these actuators requires a two-step analysis; first an electrothermal analysis to determine the temperature distribution in the device, followed by a thermostructural analysis to determine the resulting displacement field.

1.3.3.1. Electrothermal model

An electrothermal model of the device is developed to determine the temperature distribution as a function of the applied voltage. This is highly dependent upon the operating environment. When operating in air, the dominant heat transfer mechanism is heat conduction between the actuator and substrate through the air-filled gap between them.^{35,36,38} In contrast, heat dissipation by conduction through the anchors to the substrate dominates in vacuum.^{35,38} Assuming each beam is thermally independent, an electrothermal model based on a single beam is presented.³⁵ Heat transfer within the beam is treated as a one-dimensional problem since the length dimension is significantly larger than either of the cross-sectional dimensions.

First examine the case in air, where heat conduction through the air-filled gap between the actuator and substrate is the dominant mechanism of heat transfer. Here the governing equation is,

$$k_p \frac{d^2 T}{dx^2} + J^2 \rho = \frac{S}{h} \frac{T - T_s}{R_T}, \quad (1.1)$$

where k_p and ρ are the thermal conductivity and resistivity respectively of the polysilicon beams; J is the current density; $S = \frac{h}{w} \left(\frac{2h_{air}}{h} + 1 \right) + 1$ is a shape factor accounting for the effect of element shape on heat conduction

to the substrate; $R_T = \frac{h_{air}}{k_{air}} + \frac{h_n}{k_n} + \frac{h_s}{k_s}$ is the thermal resistance between the polysilicon beam and substrate; h and w are the thickness and width of a single beam respectively; h_{air} is the gap between the beam and silicon nitride layer on the substrate; h_n is the thickness of the silicon nitride; h_s is the representative thickness of the substrate; k_{air} , k_n , k_s are the thermal conductivities of air, silicon nitride, and the substrate respectively; and T_s is the temperature of the substrate.

The thermal conductivities k_p and k_{air} are both temperature dependent. However, the assumption of a constant k_p yields results similar to those using a temperature-dependent value of k_p .³⁵ Assuming a constant k_p and temperature dependent k_{air} , the finite difference method is implemented to solve (1.1) by writing the second-order differential equation in the form $\frac{d^2T}{dx^2} = b(x, T)$, and approximating it as,

$$\frac{d^2T}{dx^2} \approx \frac{1}{(\Delta x)^2} (T_{i+1} - 2T_i + T_{i-1}).$$

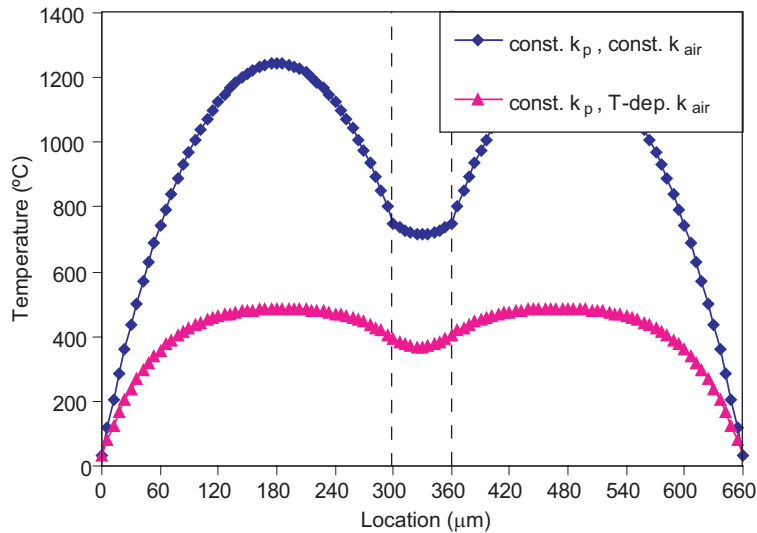


Fig. 1.3. Steady state temperature profile (with respect to the substrate) along a pair of inclined beams and the shuttle operated in air with an input current of 10 mA for both constant and temperature-dependent values of k_{air} . Locations 0-300 μm and 360-660 μm correspond to the beams while locations 300-360 μm correspond to the shuttle between the beams. The beams are anchored to the substrate at locations 0 and 660 μm .

Fig. 1.3 shows the steady-state temperature profile obtained for a two-leg (one pair of inclined beams) thermal actuator operating in air. The temperature of the shuttle is significantly lower than that of the majority of each beam. This is due to the relatively low current density in the shuttle, resulting in a lower rate of heat generation as compared to that of the beams. Furthermore, the relatively large area of the shuttle results in greater heat dissipation through the air to the substrate.

The thermal conductivity of the air has a significant effect on the actuator behavior.³⁵ This strong dependence is clearly seen in Fig. 1.3, where the only difference between the two curves is the temperature dependence of the thermal conductivity of air. k_{air} increases with temperature, increasing the heat flow between the beams and shuttle and the substrate. Consequently, the temperature of the beams and shuttle is lower for a given current flow. Clearly, decreasing heat conduction through the air increases the temperature of the beams. Ultimately, operation in vacuum maximizes the beam temperature for a given current flow, making the device more efficient.

To analyze the case where the thermal actuator operates in vacuum, remove the term for heat conduction through the air from (1.1),

$$k_p \frac{d^2 T}{dx^2} + J^2 \rho = 0.$$

Fig. 1.4 shows that the highest temperature now occurs in the shuttle rather than in the beams. Here the temperature depends most upon the distance from the anchor points which are now assumed to be the only source of heat dissipation. Since the shuttle is furthest from the anchors, it reaches the highest temperature.

1.3.3.2. *Thermomechanical model*

With the temperature distribution now known from the electrothermal analysis, the thermomechanical behavior of the actuator is modeled to determine the resulting displacement. The following assumptions are made in the analytical derivation of the thermomechanical behavior:

- the average temperature increase in the inclined beams is known;
- deformation of the central shuttle is negligible compared to that of the inclined beams;
- all strains and displacements are small, and;
- there is negligible shear deformation of the beams.

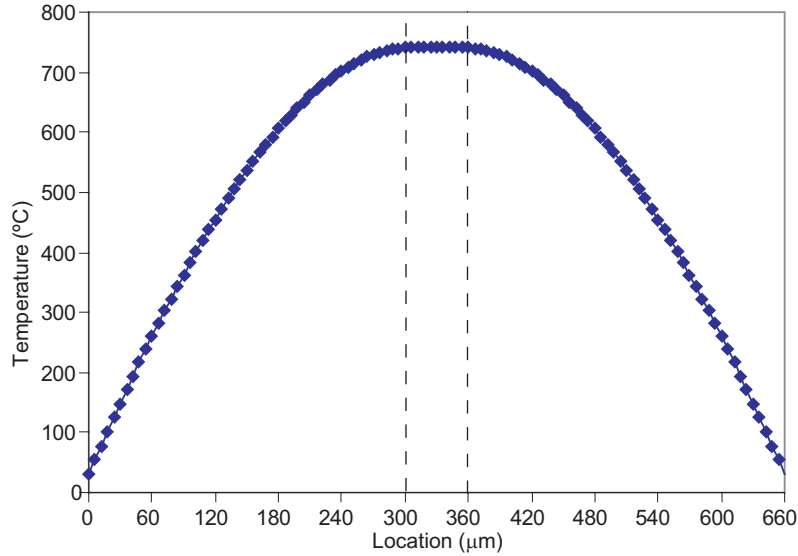


Fig. 1.4. Steady state temperature profile along a pair of inclined beams and the shuttle operated in vacuum with an input current of 3 mA. The thermal conductivity of polysilicon is assumed temperature dependent. Locations 0-300 μm and 360-660 μm correspond to the beams while locations 300-360 μm correspond to the shuttle between the beams. The beams are anchored to the substrate at locations 0 and 660 μm .

As in the electrothermal analysis, a single pair of inclined beams is first considered as shown in Fig. 1.5a. Later the entire device, including the thermal actuator, specimen, and load sensor is analyzed.

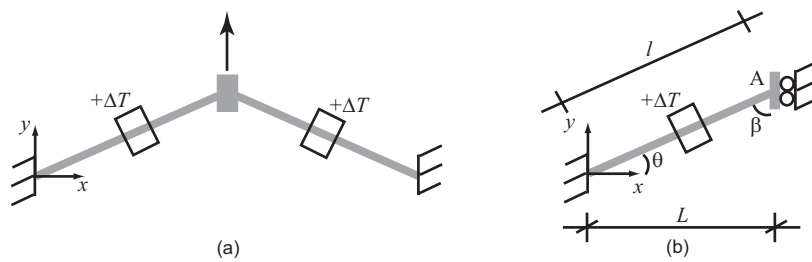


Fig. 1.5. Schematic of a pair of inclined beams subjected to an average increase in temperature ΔT . (a) Two beams joined at the central shuttle; (b) Equivalent mechanical representation of a single beam.

The pair of inclined beams, forming a single V-shaped clamped beam, is subjected to a uniform increase in temperature along its length. While the thermomechanical response of a similar structure was previously approximated,³⁹ the following analysis follows a rigorous structural mechanics approach.

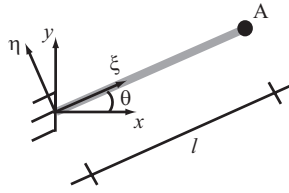


Fig. 1.6. Schematic of an inclined beam in a local reference frame.

Exploiting the symmetry of the system, the mechanical response is equivalently computed considering half of the structure as shown in Fig. 1.5b. To determine the axial force in the beam and the displacement of Node A (Fig. 1.5) in the y -direction, the elastic stiffness matrix of the beam is assembled relative to the displacements in Node A. Before obtaining the stiffness matrix in the global frame, it is first computed in a local reference frame as shown in Fig. 1.6. The governing structural equations for the beam subjected to an average temperature increase ΔT are,²⁵

$$\begin{bmatrix} \frac{EA}{l} & 0 \\ 0 & 12\frac{EI}{l^3} \end{bmatrix} \begin{bmatrix} U_{\xi}^A \\ U_{\eta}^A \end{bmatrix} = \begin{bmatrix} \alpha\Delta T EA \\ 0 \end{bmatrix} + \begin{bmatrix} R_{\xi}^A \\ R_{\eta}^A \end{bmatrix}, \quad (1.2)$$

where E , A , and l are the Young's modulus, cross-sectional area, and length of the beam respectively; I is the moment of inertia of the beam with respect to the out-of-plane axis ζ in the local reference frame; U_{ξ}^A and U_{η}^A are the displacements of Node A in the directions ξ and η respectively; α is the coefficient of thermal expansion of the beam material; and R_{ξ}^A and R_{η}^A are the reaction forces at Node A in directions ξ and η respectively.

The boundary conditions are known in terms of the global x - y reference frame in Fig. 1.5. Thus (1.2) is transformed to the global system by a rotation matrix relating the local and global degrees of freedom,

$$\begin{bmatrix} U_{\xi}^A \\ U_{\eta}^A \end{bmatrix} = \begin{bmatrix} \cos \theta & \sin \theta \\ -\sin \theta & \cos \theta \end{bmatrix} \begin{bmatrix} U_x^A \\ U_y^A \end{bmatrix}.$$

Applying this relation, (1.2) becomes,

$$\begin{bmatrix} c^2 \frac{EA}{l} + s^2 \frac{12EI}{l^3} & cs \left(\frac{EA}{l} - \frac{12EI}{l^3} \right) \\ cs \left(\frac{EA}{l} - \frac{12EI}{l^3} \right) & s^2 \frac{EA}{l} + c^2 \frac{12EI}{l^3} \end{bmatrix} \begin{bmatrix} U_x^A \\ U_y^A \end{bmatrix} = \begin{bmatrix} \alpha \Delta T EA c \\ \alpha \Delta T EA s \end{bmatrix} + \begin{bmatrix} R_x^A \\ R_y^A \end{bmatrix}, \quad (1.3)$$

where $c = \cos \theta$ and $s = \sin \theta$. The boundary conditions reflecting the constraint at Node A are $U_x^A = 0$, $R_x^A \neq 0$, $U_y^A \neq 0$, and $R_y^A = 0$. Applying these to (1.3) yields the reaction force on Node A in the x -direction and the displacement of Node A in the y -direction for an average increase in temperature ΔT along the beam, namely;

$$R_x^{\Delta T} \equiv R_x^A = -\alpha \Delta T EA \frac{c}{s^2 \frac{Al^2}{12I} + c^2} \equiv -\alpha \Delta T EA \frac{c}{s^2 \Psi + c^2} \quad (1.4)$$

$$U^{\Delta T} \equiv U_y^A = \alpha \Delta T l \frac{s}{s^2 + c^2 \frac{12I}{Al^2}} \equiv \alpha \Delta T l \frac{s}{s^2 + \frac{c^2}{\Psi}}. \quad (1.5)$$

Here the dimensionless parameter $\Psi = Al^2/12I$ represents the ratio of the axial and bending stresses. Using the reaction force R_x^A , it is possible to obtain the compressive axial force N in the beam by projection along the axial direction, $N = R_x^A c$. A similar analysis yields the response of a pair of inclined beams subjected to an external force F applied to the central shuttle acting in the y -direction. In this case, the axial internal force and displacement of Node A are determined using the same system of governing equations (1.3) by replacing the vector on the right hand side that depends on the temperature increase with the external applied force vector $[0 \ F/2]^T$. The axial force and displacement now become,

$$R_x^F \equiv R_x^A = cs \left(\frac{EA}{l} - \frac{12EI}{l^3} \right) U_y^A = F \frac{cs(\Psi - 1)}{2(s^2 \Psi + c^2)},$$

$$U^F \equiv U_y^A = F \frac{1}{2(s^2 \frac{EA}{l} + c^2 \frac{12EI}{l^3})} = \frac{Fl}{EA} \frac{1}{2(s^2 + \frac{c^2}{\Psi})}.$$

Using the displacement U^F for a given force F , the stiffness of the V-shaped clamped thermal beam shown in Fig. 1.5 is,

$$K_{tb} \equiv \frac{F}{U^F} = 2 \left(s^2 + \frac{c^2}{\Psi} \right) \frac{EA}{l}.$$

A more realistic situation is one where the V-shaped beam experiences both a temperature increase ΔT applied to actuate the device as well as an external force F in reaction to the displacement. This displacement is,

$$U^{\Delta T + F} = U^{\Delta T} + U^F = \frac{2\alpha \Delta T EA s + F}{K_{tb}}.$$

In the MEMS-based tensile loading device, a number of heat sink beams running between the shuttle and substrate are placed near the specimen to reduce the influence of the thermal actuator on the temperature of the specimen (see for example Fig. 1.8). Each pair of heat sink beams has a stiffness in the direction of the shuttle motion of²⁵

$$K_{sb} = 2 \frac{12EI_{sb}}{l_{sb}^3} = \frac{2Eb_{sb}^3h}{l_{sb}^3},$$

where I_{sb} , l_{sb} , and b_{sb} are the moment of inertia, length, and width of the heat sink beams respectively.

Finally, combining all these factors to make a thermal actuator with m pairs of thermal beams and n pairs of heat sink beams, the total stiffness and shuttle displacement are:

$$K_{TA} = mK_{tb} + nK_{sb} \tag{1.6}$$

$$U_{TA} = \frac{U^{\Delta T}mK_{tb} + F}{K_{TA}} = \frac{2m\alpha\Delta TEAs + F}{K_{TA}}, \tag{1.7}$$

where $U^{\Delta T}$, given by (1.5), is the displacement of the actuator in the absence of heat sink beams. Here the relation for the displacement is obtained by imposing compatibility in the kinematics of the systems of the thermal and heat sink beams.

1.3.3.3. Thermomechanical response of entire loading device

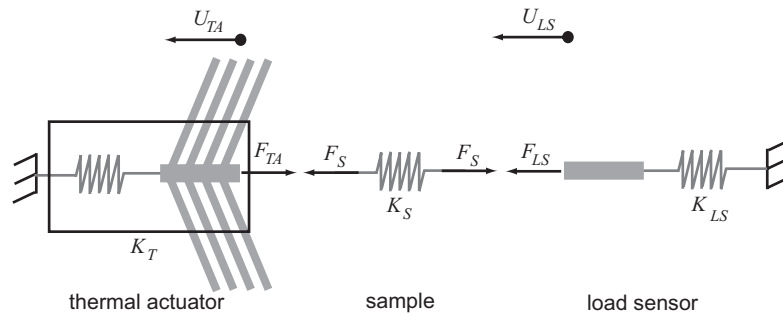


Fig. 1.7. Lumped model of the entire tensile loading device with internal forces and displacements shown in free body form.

With the mechanical response of the thermal actuator known for a given current input, it is now possible to formulate a set of equations governing the behavior of the entire device. A lumped model of the entire device

is constructed as shown in Fig. 1.7. Here K_S is the stiffness of the tensile specimen, K_{LS} is the stiffness of the load sensor corresponding to the folding beams by which it is suspended, K_{TA} is the stiffness of the thermal actuator computed in (1.6), and U_{LS} is the displacement of the load sensor. The central shuttle is assumed to be rigid.

The governing equations for the lumped system shown in Fig. 1.7 are given by:²⁵

$$\begin{aligned}
 \Delta U_S &= U_{TA} - U_{LS} \\
 U_{TA} &= \frac{2m\alpha\Delta TEAs - F_{TA}}{K_{TA}} \\
 F_{TA} &= F_S = F_{LS} \\
 F_S &= K_S\Delta U_S \\
 F_{LS} &= K_{LS}U_{LS},
 \end{aligned} \tag{1.8}$$

where $s = \sin\theta$ and ΔU_S is the elongation of the specimen. Solving the system (1.8), the displacement of the thermal actuator U_{TA} , the tensile force on the specimen F_S , the elongation of the specimen ΔU_S , and the corresponding displacement of the load sensor U_{LS} are obtained:

$$\begin{aligned}
 U_{TA} &= \frac{2m\alpha\Delta TEAs}{K_{TA} + K_{TA}K_{LS}/K_S + K_{LS}} + \frac{2m\alpha\Delta TEAs}{K_{TA} + K_S + K_{TA}K_S/K_{LS}} \\
 F_S &= \frac{2m\alpha\Delta TEAs}{K_{TA}/K_S + 1 + K_{TA}/K_{LS}} \\
 \Delta U_S &= \frac{2m\alpha\Delta TEAs}{K_{TA} + K_S + K_{TA}K_S/K_{LS}} \\
 U_{LS} &= \frac{2m\alpha\Delta TEAs}{K_{TA} + K_{TA}K_{LS}/K_S + K_{LS}}.
 \end{aligned} \tag{1.9}$$

These represent the critical parameters in obtaining force-displacement data using the MEMS-based tensile loading device.

1.3.4. Multiphysics FEA of the thermal actuator

While the displacement of the actuator in vacuum is easily characterized experimentally,²⁵ the temperature distribution is more difficult to obtain. Therefore a coupled-field simulation is particularly necessary. This analysis also helps to assess the temperature at the actuator-specimen interface and to examine the effectiveness of the thin heat sink beams in controlling the temperature increase of the specimen during actuation.

The MEMS-based tensile stage is intended to operate within the SEM or TEM. Thus the following finite element electrothermal analysis is carried out for the case where the device operates in vacuum. The actuation voltage applied across the anchor points serves as the input while the output includes both the actuator temperature and displacement fields. Displacements at the anchor points are held fixed in the mechanical boundary conditions. The thermal boundary conditions are zero temperature change at the anchors.

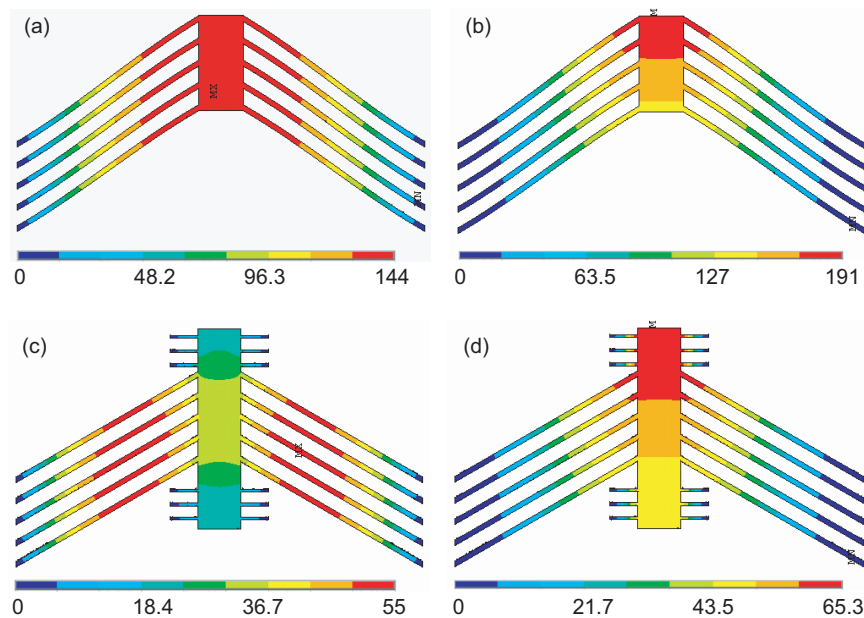


Fig. 1.8. (a) Temperature increase ($^{\circ}\text{C}$) and (b) displacement field (nm) in the thermal actuator. The displacement component plotted is in the shuttle axial direction. (c) Temperature ($^{\circ}\text{C}$) and (d) displacement field (nm) in the thermal actuator with three pairs of heat sink beams at the specimen end. In this analysis, the heat sink beams are $40\ \mu\text{m}$ in length and $4\ \mu\text{m}$ wide with $16\ \mu\text{m}$ spacing between them. ANSYS Multiphysics, version 6.1 was used in this analysis.

Fig. 1.8a,b depicts the temperature and displacement in the thermal actuator for an actuation voltage of 1 V. As previously described, heat dissipation through the anchors is the dominant dissipation mechanism. Since the shuttle is furthest from the anchors, the highest temperature occurs in the shuttle. Due to the nonuniformity of the temperature distribution, the displacement is also nonuniform.

Heating of the specimen during actuation is unavoidable as a result of the increased temperature of the shuttle to which the sample is attached. However, this effect is minimized with the addition of a series of heat sink beams running between the shuttle and substrate near the shuttle-specimen interface as shown in Fig. 1.8c,d. To avoid out-of-plane bending, another three pairs of heat sink beams are placed at the opposite end of the shuttle. Comparing this to the case without the heat sink beams (Fig. 1.8a,b), this configuration allows for more than twice the displacement at the specimen end of the shuttle for the same allowable temperature increase at the shuttle-specimen interface. The problem of specimen heating can be further mitigated with the addition of a thermal isolation layer between the actuator and specimen following the custom microfabrication process³⁸ for highly temperature-sensitive samples.

1.3.5. Buckling analysis

For large tensile loads, buckling of the inclined beams in the thermal actuator is a concern. This occurs in the plane of minimum moment of inertia when the internal force exceeds the critical buckling load. Depending on the beam dimensions, this plane can be either parallel or orthogonal to the surface of the substrate. In this analysis, each beam is assumed to be fixed at the end where it is anchored to the substrate, while it is able to translate along the shuttle's axial direction with no rotation at the other end. The critical axial force at which buckling occurs is:

$$P_{cr} = \pi^2 \frac{EI_{min}}{l^2}. \quad (1.10)$$

For an unloaded thermal actuator (disconnected from the sample and any heat sink beams), the axial internal force is $R_x^{\Delta T} c = \alpha \Delta T E A \frac{c^2}{s^2 \Psi + c^2}$ where $R_x^{\Delta T}$ is given by (1.4). For an actuator connected to a tensile sample, heat sink beams, and load sensor, the maximum possible axial force achieved is $\alpha \Delta T E A$, i.e. when the actuator is attached to an elastic system of infinite stiffness and cannot translate. The true axial force experienced by the beams during operation falls somewhere between the two extremes.

1.3.6. Evaluating the analytic and finite element models

The thermal actuator is calibrated experimentally to verify the analytical and FEA models described above. Fig. 1.9²⁵ shows a comparison the analytical and FEA predictions of actuator displacement for a given current

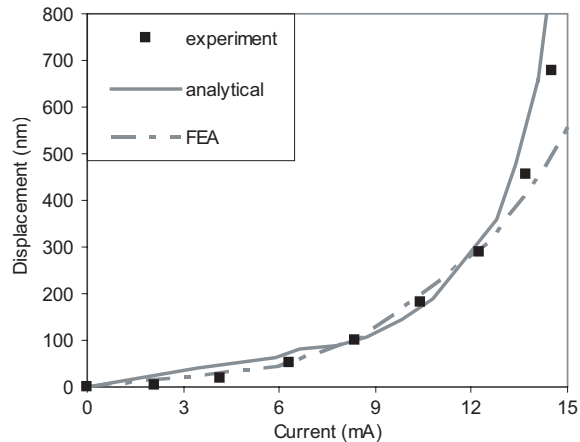


Fig. 1.9. Comparison of displacement at the actuator-specimen interface as predicted by the analytical and FEA models and measured experimentally. Displacement is plotted as a function of the input current. Each experimental point is the average of three experimental measurements obtained from different but geometrically identical thermal actuators.

input with experimentally-measured results. The displacement of the actuator was measured in the SEM,²⁶ giving spatial resolution of better than 5 nm. Using the analytical model, the displacement is computed based on experimentally-measured temperatures in the actuator.²⁵ As mentioned in Sec. 1.3.4, the input to the multiphysics model is the voltage applied across the anchor points of the thermal actuator. In order to obtain the resulting current, the resistance of the actuator is computed using the output temperature and a value of resistivity corresponding to the average temperature of the device.²⁵

The models agree well with the experimentally-measured actuator displacements as shown in Fig. 1.9. This suggests the models are useful in predicting the behavior of thermal actuators of other geometry. At large currents (above approximately 12 mA), both the analytical and FEA models deviate slightly from the experimental results. This can be explained largely by inaccuracies in material parameters such as resistivity and thermal conductivity at high temperature.^{29,35} Furthermore, the microstructure of polysilicon begins to be modified at these high current levels and elevated temperatures.²⁵

1.3.7. Load sensor

The load sensor consists of a differential capacitive displacement sensor suspended on a set of elastic members of known stiffness. By calibrating the stiffness of the sensor,^{26,40} the load is computed based on the measured displacement. The differential capacitive displacement sensor^{41–43} is chosen for its sensitivity and linear behavior over a range of displacements appropriate for tensile testing of nanostructures.

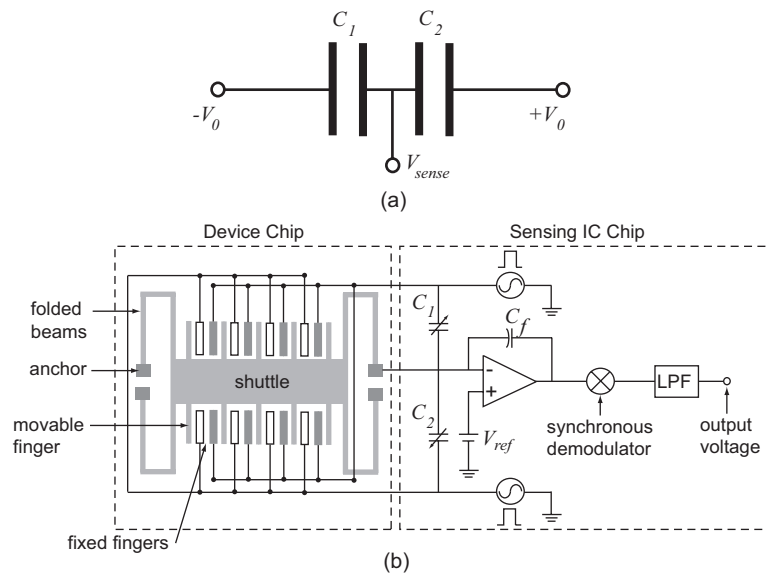


Fig. 1.10. (a) A simple model of the differential capacitor. (b) Double chip architecture used for measuring capacitance change. The capacitance change is proportional to the output voltage change.

The differential capacitive sensor is comprised of a movable rigid shuttle with electrodes (or “fingers”) pointing outward as shown schematically in Fig. 1.10.²⁶ These fingers are interdigitated between pairs of stationary fingers (Fig. 1.10b) fixed to the substrate. Under no load, each movable finger sits centered between the two stationary fingers. Each set of fingers (one movable and a stationary on either side) forms two capacitors, one between the movable finger and each stationary finger. The entire capacitance sensor is equivalent to two combined capacitances, C_1 and C_2 , as

shown in Fig. 1.10a, namely,

$$C_1 = C_2 = C_0 = \epsilon N \frac{A}{d_0} (1 + f),$$

where ϵ is the electric permittivity, N is the number of movable fingers, A and d_0 are the area of overlap and initial gap respectively between the movable finger and each stationary finger, and $f = 0.65d_0/h$ is the fringing field correction factor with h being the beam height.⁴⁴

The movable fingers are attached to the folded beams via the rigid movable shuttle so their displacements are equivalent. This displacement yields a change in capacitance given by,

$$\Delta C = C_1 - C_2 = N\epsilon A \left(\frac{1}{d_0 - \Delta d} - \frac{1}{d_0 + \Delta d} \right) \approx \frac{2N\epsilon A}{d_0^2} \Delta d,$$

where Δd is the displacement of the load sensor. Note the fringing effect factor cancels. For displacements Δd within 50% of the initial gap d_0 , the capacitance changes approximately linearly with the sensor displacement. This relatively large range of linear sensing is a major advantage of differential capacitance sensing over direct capacitance sensing which uses a single fixed beam for each movable beam.

A variety of circuit configurations may be used in measuring capacitance.^{41,42} Fig. 1.10 shows schematically the charge sensing method used in the device described in this chapter. This method mitigates the effects of parasitic capacitances that generally occur in electrostatic MEMS devices. Here the change in output voltage ΔV_{sense} is proportional to the capacitance change,

$$\Delta V_{sense} = \frac{V_0}{C_f} \Delta C,$$

where V_0 is the amplitude of an AC voltage signal applied to the stationary fingers and C_f is the feedback capacitor shown in Fig. 1.10.

Minimizing stray capacitance and electromagnetic interference is critical in high resolution capacitance measurements. In this case, integrating the MEMS differential capacitor and sensing electronics on a single chip would minimize these effects, allowing detection of changes in capacitance at the atto-Farad level.⁴² However, this would greatly increase fabrication complexity. The double chip architecture depicted in Fig. 1.10 is an alternative to the single chip scheme. Here the MEMS-based system is fabricated on one chip while a commercial integrated circuit chip (for example, Universal Capacitive Readout MS3110, Microsensors, Costa Mesa, CA) is used to

measure changes in capacitance. Both chips are housed on a single printed circuit board.

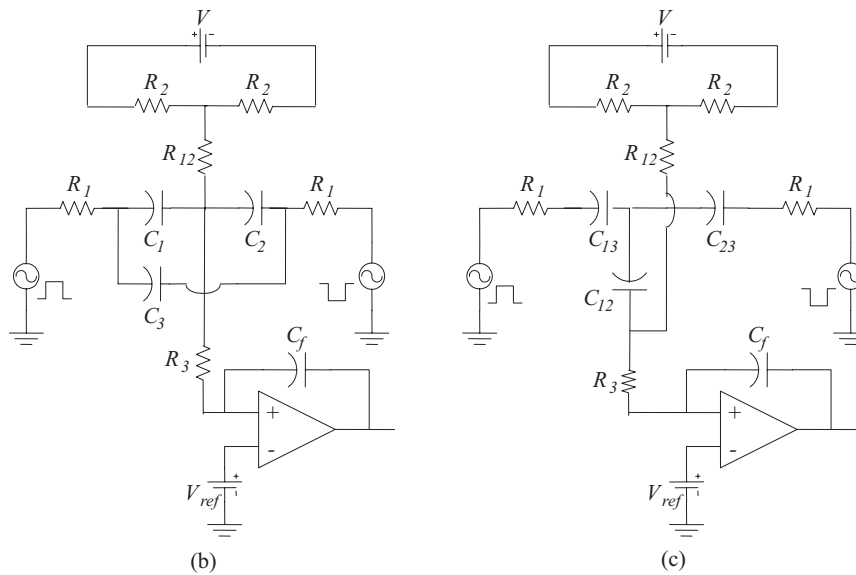
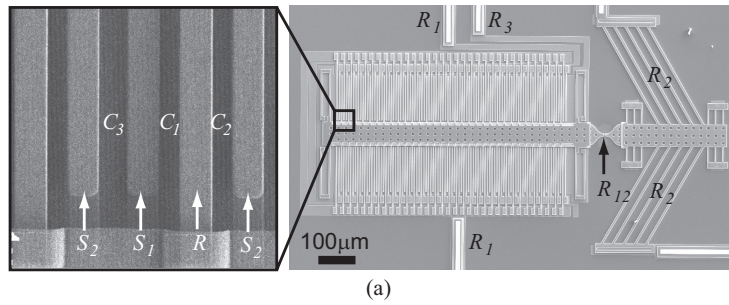


Fig. 1.11. (a) The device with an electrothermal actuator and corresponding resistances and capacitances. The inset shows details of the movable and stationary fingers. R_2 denotes the resistance of thermal beams, R_{12} the resistance of specimen, R_1 and R_3 the resistances of electric traces, C_1 and C_2 the capacitances between the movable beams and the two stationary beams, respectively, and C_3 the capacitance between two nearby stationary beams. (b) Equivalent electric circuit for the device in (a). (c) Equivalent circuit to that in (b) after a $\Delta - Y$ transformation.

An equivalent circuit for the entire device, including the electrothermal actuator, is shown in Fig. 1.11. The load sensor shuttle is connected elec-

trically to the substrate through the anchor points. The capacitances are given by,

$$C_1 = N\epsilon \left(\frac{A_1}{d_0 + \Delta d} + \frac{A_2}{g} + 0.65 \frac{A_1}{h} \right), \quad (1.11)$$

$$C_2 = N\epsilon \left(\frac{A_1}{d_0 - \Delta d} + \frac{A_2}{g} + 0.65 \frac{A_1}{h} \right), \quad (1.12)$$

$$C_3 = N\epsilon \left(\frac{A_1}{d_3} + 0.65 \frac{A_1}{h} \right), \quad (1.13)$$

where N is the total unit number of differential capacitors, A_1 is the overlapping area of the stationary finger with the movable finger, A_2 is the overlapping area of the stationary finger with the substrate, d_0 is the gap between the stationary finger and the movable finger, Δd is the displacement of the movable finger, d_3 is the gap between the two stationary fingers, g is the gap between the fixed finger and substrate, and h is the finger thickness. In (1.11) and (1.12), the first term represents the capacitance between each fixed finger and the corresponding movable finger. The second term is the capacitance between the fixed finger and the shield beneath the load sensor which is held at the same potential as the movable finger. The third term considers the fringe effect. Note that when $\Delta d = 0$, $C_1 = C_2 \equiv C_0$.

The capacitance term from the fringe effect C_3 cannot be neglected as d_3 is typically comparable to d_0 . Fig. 1.11b shows the circuit used for the device in Fig. 1.11a while Fig. 1.11c shows the equivalent circuit due to a $\Delta - Y$ transformation.⁴⁵ Here the equivalent capacitances are given by,

$$\begin{aligned} C_{13} &= \frac{C_1 C_2 + C_2 C_3 + C_3 C_1}{C_2} \\ C_{23} &= \frac{C_1 C_2 + C_2 C_3 + C_3 C_1}{C_1} \\ C_{12} &= \frac{C_1 C_2 + C_2 C_3 + C_3 C_1}{C_3} \end{aligned} \quad (1.14)$$

Combining (1.11-1.13) and (1.14) gives the difference in capacitance,

$$\begin{aligned} C_{13} - C_{23} &= N\epsilon_0 A_1 \left(1 + \frac{C_1 + C_2}{C_1 C_2} \right) \left(\frac{1}{d_0 + \Delta d} - \frac{1}{d_0 - \Delta d} \right) \\ &\approx 2N\epsilon_0 A_1 \frac{1 + 2C_3/C_0}{d_0^2} \Delta d, \end{aligned} \quad (1.15)$$

$$C_{12} = C_1 + C_2 + \frac{C_1 C_2}{C_3} \approx 2C_0 + \frac{C_0^2}{C_3} = \text{constant}. \quad (1.16)$$

These capacitance values agree well with those obtained in FEA simulation.⁴⁶ The quantity $C_{13} - C_{23}$ in (1.15) is the capacitance that is measured experimentally while using the MEMS tensile loading device. This is approximately five times greater than the quantity $C_1 - C_2$, which is advantageous in measuring sub-femtoFarad capacitances. In practice, the displacement-capacitance relation is calibrated experimentally²⁶ for improved accuracy.

1.4. Design criteria

Taking into consideration the above analyses, the following design criteria are set to achieve an effective and reliable material testing system:

- (1) Large load sensor displacements to maximize load resolution;
- (2) Low temperature at the actuator-specimen interface to avoid artificial heating of the specimen;
- (3) The testing system operates as a displacement control, i.e., the stiffness of the thermal actuator is significantly higher than that of the specimen and load sensor, and;
- (4) The actuator does not buckle within the operational temperature range.

The specimen stiffness, failure load, and elongation at failure (ΔU_S) dictate the choice of actuator geometry and the number and dimensions of the beams. Consequently, optimization of the device design requires some preliminary knowledge of the specimen behavior as is customary in experimental mechanics.

In choosing the stiffness of the load sensor (K_{LS}), a compromise between the maximum force applied to the specimen and sensor displacement must be reached. The force applied to the specimen is $F_S = F_{LS} = K_{LS}U_{LS}$. For a differential capacitance load sensor, the displacement resolution remains approximately constant.²⁶ Thus the smaller the stiffness, the greater the load resolution. However, in order to achieve the required elongation of the sample ΔU_S for failure, the displacement of the thermal actuator U_{TA} must increase. This in turn requires higher temperatures resulting in greater heating of the specimen.

The displacement of the thermal actuator (unconstrained by heat sink beams or a specimen) depends on the beam length l , beam angle θ , temperature increase, and stiffness ratio Ψ given in (1.5). The longer the beams, the greater the displacement. However, longer beams are more likely to stick to the substrate during microfabrication and are more prone to buck-

ling. Thus there is a practical limit placed on the length of the inclined beams.

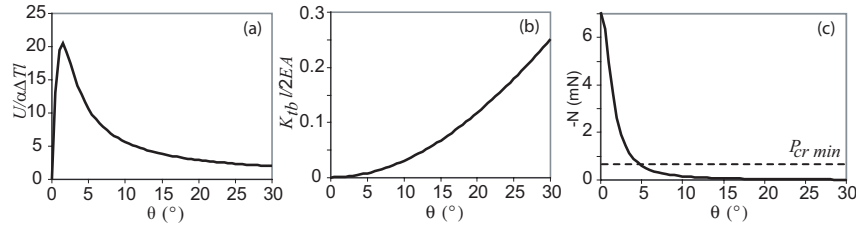


Fig. 1.12. Important parameters in the device design as functions of the thermal beam angle: (a) displacement; (b) stiffness of the thermal actuator; and (c) internal stress. The parameters in (a) and (b) are plotted as dimensionless quantities. Beam dimensions of length $l = 300 \mu\text{m}$, width $b = 8 \mu\text{m}$ and height $h = 3.5 \mu\text{m}$ were chosen.

Fig. 1.12a²⁵ shows the displacement of the thermal actuator as given by (1.5) as a function of the beam angle. Here the displacement is plotted as a dimensionless quantity $(U^{\Delta T}/\alpha\Delta Tl)$ for a fixed stiffness ratio of $\Psi = 1406$. The displacement increases with a decrease in the beam angle in the range $\theta > 2^\circ$. Thus to obtain a given displacement, an actuator with a smaller beam angle ($\theta > 2^\circ$) requires a smaller temperature increase and equivalently a smaller actuation voltage.

Regarding the third design criterion, it is desirable to have the thermal actuator operate in displacement control mode. The ability to prescribe the displacement of the tensile specimen is critical in mechanical testing. This allows important mechanical phenomena such as stress softening and fracture to be captured. In order to achieve true displacement control, the actuator would ideally have infinite stiffness, allowing it to reach the desired displacement regardless of the required force (in theory, it could apply infinite force if given infinite stiffness). In practice, the actuator stiffness must be significantly larger than that of the specimen and load sensor. Fig. 1.12b plots the stiffness of the thermal actuator as a function of beam angle for the same fixed stiffness ratio ($\Psi = 1406$). Again the quantities are plotted in dimensionless form with the dimensionless stiffness being $K_{tb}l/2EA$. Contrary to the inverse relationship between actuator displacement and beam angle, the actuator stiffness increases with beam angle. Thus there is a trade off between maximizing the displacement and stiffness of the actuator.

The final design criterion considers the possibility of buckling. As the temperature of the beams rises, the internal forces build, increasing the possibility of buckling. Fig. 1.12c plots the internal axial force as a function of the beam angle as well as the critical minimum buckling force for a temperature increase of $\Delta T = 800$ K. Since the recrystallization temperature of polysilicon (the material of the beams) is approximately 800 K,⁴⁷ the beams are not expected to buckle within the functional temperature range. The plot shows that the actuator buckles when the beam angle is less than approximately 5° at 800 K.

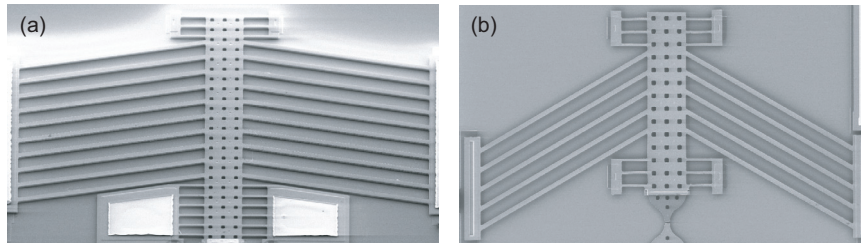


Fig. 1.13. Two types of thermal actuators for testing various types of nanostructures. (a) 10 pairs of thermal beams with beam angle of 10° ; (b) 5 pairs of thermal beams with a beam angle of 30°

To summarize, an actuator with a small beam angle requires the lowest temperature increase for a given displacement. However, the structural stability of the actuator decreases with beam angle. For specimens requiring large actuator displacements, a beam angle of 10° may be selected (Fig. 1.13a). For specimens requiring only moderate displacements and greater forces, a beam angle of 30° is more appropriate (Fig. 1.13b). In each case, the number of thermal beams is chosen to achieve the desired actuator stiffness-to-load sensor stiffness and actuator stiffness-to-specimen stiffness ratios. Likewise, the load sensor stiffness is chosen according to (1.8) and (1.9) once an estimate of the specimen stiffness and elongation at failure is made.

1.5. Material testing

The MEMS-based tensile stage can be used to test nanometer-scale materials and structures ranging from nanowires and nanotubes to ultra-thin films. As the structures shrink below the sub-micron and into the nanometer scale, new mechanisms dominate their mechanical behavior. For in-

stance, nanowires and nanotubes possess a relatively large surface area-to-volume ratio. Consequently, interfaces, interfacial energy, and surface topography play an increasingly important role in their deformation and failure processes. In larger structures, generation and motion of dislocations dictates material behavior. As grain sizes or structural dimensions fall below 50 to 100 nm, surface and intermolecular mechanisms gain influence over material behavior. Therefore understanding the mechanics of these new materials and structures is essential. As an example, the following briefly demonstrates the use of the MEMS-based tensile stage for in-situ SEM and TEM of testing nano-scale polysilicon films, palladium nanowires, and multi-walled carbon nanotubes.

1.5.1. *Sample preparation*

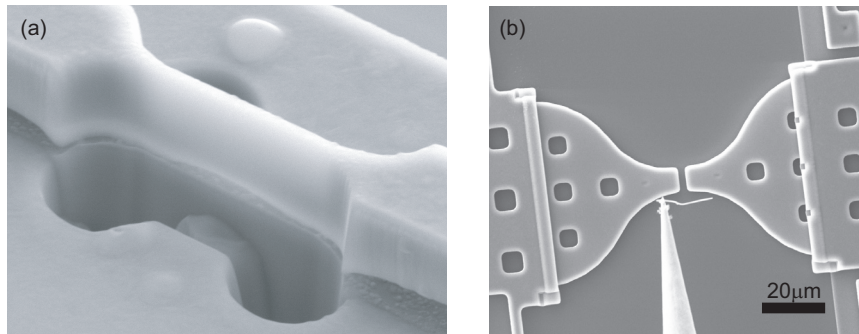


Fig. 1.14. Sample preparation. (a) A polysilicon thin film tensile specimen cofabricated with the MEMS device and further thinned by FIB machining. (b) A palladium nanowire being manipulated into place on the MEMS device using a tungsten probe and nanomanipulator.

The size and fragile nature of nano-scale materials and structures demands specialized techniques for preparation and mounting on the MEMS device. Thin films may be cofabricated with the MEMS device. This eliminates any handling. For example, freestanding polysilicon films were cofabricated with the MEMS device between the actuator and the load sensor (Fig. 1.14a).²⁴ Due to limitations in the resolution of the photolithography used to make the devices, the initial film thickness could not be made thinner than approximately 2 μm . To reduce the thickness dimension, the polysilicon specimen is further machined by focused ion beam (FIB) down to 350-450 nm.

Individual nanowires and nanotubes may either be grown across the gap between the actuator and load sensor or placed by nanomanipulator²⁴ as shown in Fig. 1.14b. This procedure involves use of a nanomanipulator operated within an SEM to pick up and place an individual nanostructure across the gap, followed by electron beam-induced deposition (EBID) of platinum to weld the ends of the structure in place.

1.5.2. Tensile tests

1.5.2.1. Tensile tests of polysilicon thin films

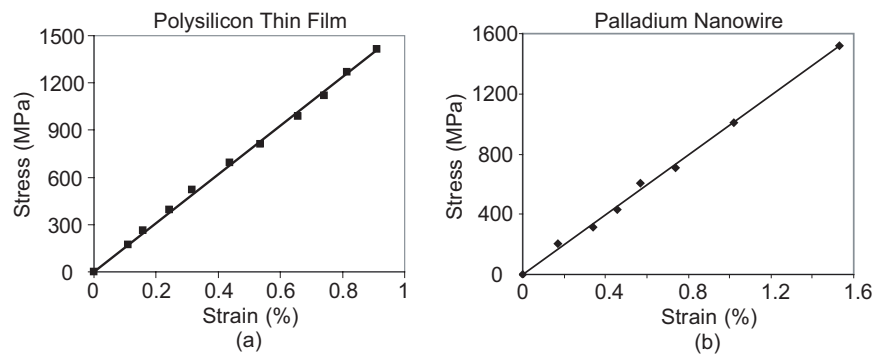


Fig. 1.15. Stress-strain data for (a) a polysilicon thin film specimen²⁵ and (b) a palladium nanowire.²⁴

Thin film specimens cofabricated with the MEMS device were tested in the SEM. The results of a tensile test of a polysilicon specimen prepared as described in 1.5.1 are shown in Fig. 1.15a. Here the stress-strain curve shows strong linearity with a Young's modulus of 156 ± 17 GPa.²⁵ This result is consistent other reported values for polysilicon films.^{11,46,48}

1.5.2.2. Tensile tests of nanowires

The tensile test of a palladium nanowire, shown in Fig. 1.15b,²⁴ reveals an interesting point. The nanowire was stressed to 1.5 GPa, significantly higher than the yield stress of bulk nanocrystalline Pd,⁴⁹ and remained elastic without fracture. This phenomenon, which is attributed to the high stress threshold for the nucleation of defects,^{50,51} confirms that the strength of the material increases as its scale decreases. Ultimately, the

strength should tend to approach the theoretical strength of the material (approximately 1/10 of its Young's modulus).⁴⁹

1.5.2.3. *Tensile tests of carbon nanotubes and the effects of irradiation*

In-situ SEM and TEM tensile tests of multi-walled carbon nanotubes using the MEMS device allow insight into their failure mechanisms. Fig. 1.16 shows sequential SEM images of the in-situ SEM tensile testing of a MWNT. In this case, fracture occurs in a typical "sword-in-sheath" fashion.¹² It is possible that the outermost shell breaks and subsequently the inner concentric shells telescope out. However, the instrument resolution does not permit identification of single or multiple shell failure. As described in 1.5.1, the two ends of the outermost shell are clamped to the testing device using EBID of platinum.²⁴ Consequently, it is reasonable to assume that the outermost shell carries the load and breaks under tensile loading as only van der Waals interactions between the concentric inner shells are expected. Based on the assumption that there is minimal load transfer between the outermost shell and subsequent inner shells, stress and strain are often calculated using the measured outer diameter of the MWNT and an assumed shell thickness of 0.34 nm (equal to the interlayer distance of 0.34 nm),^{13,52} as opposed to using the combined thickness of multiple concentric shells.

In contrast to tests of unmodified MWNTs, in-situ TEM tensile tests of MWNTs exposed to high-energy electron or ion beam irradiation reveal that multiple shells or the entire cross section break simultaneously, resulting in greater stiffness.⁴⁰ This observation suggests that the irradiation introduces crosslinks between shells, resulting in load transfer. A series of tests demonstrating this effect were performed using the MEMS device on MWNTs exposed to varying degrees of ion or electron beam radiation, as well as on unexposed MWNTs as a control.⁴⁰ These tests are summarized in Fig. 1.17 and Tab. 1.1. Here it is important to note that the irradiation energy of the electron beam used for SEM imaging during mounting of the MWNTs on the MEMS device is well below the threshold for atomic structure modification and thus is assumed to have negligible effect relative to the high-energy electron and ion beam exposure.

MWNTs exposed to ion irradiation demonstrated significantly greater stiffness than those that were not.⁴⁰ In Test 1 (see Tab. 1.1), the MWNT was irradiated with Ga⁺ ions at a flux of 10^{13} e cm⁻²s⁻¹ for 10 seconds

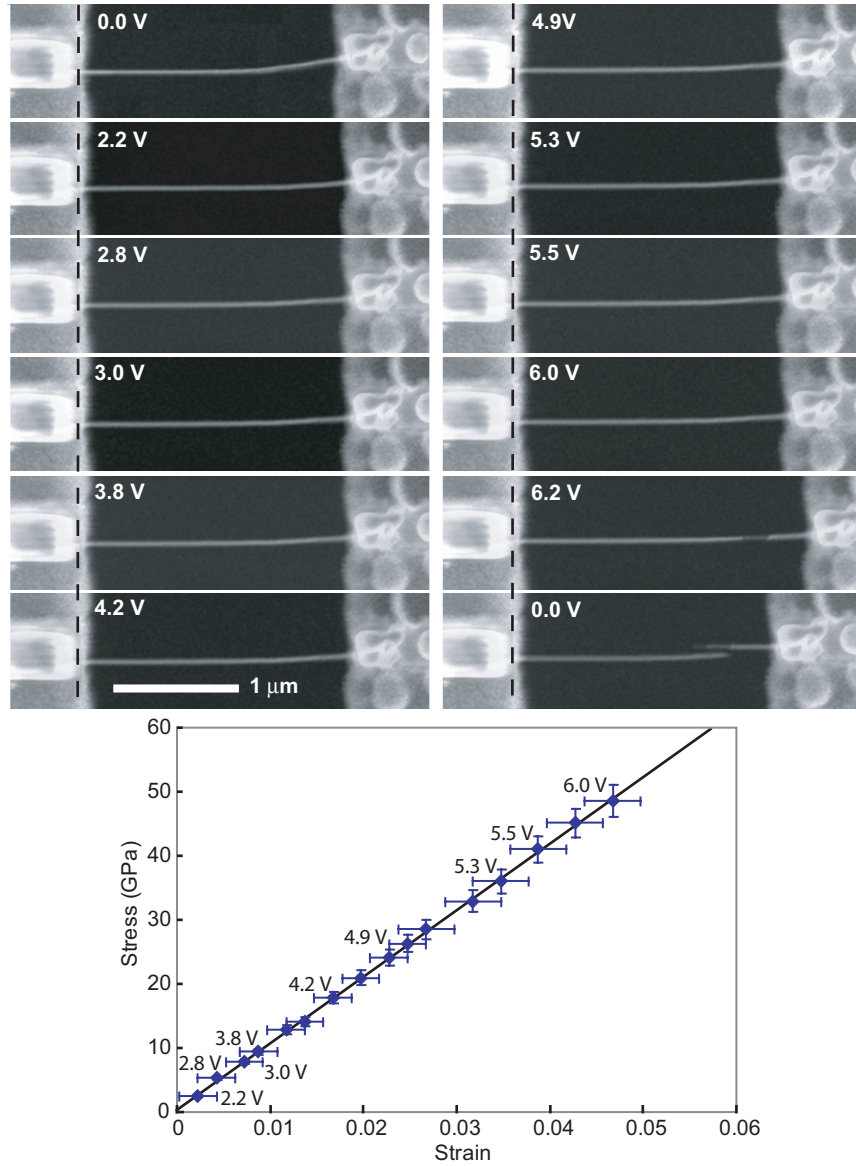


Fig. 1.16. Sequential SEM images and corresponding stress-strain data of a tensile test of a multi-walled carbon nanotube. The nanotube is 2 μm in length and 42 nm in diameter.

Table 1.1. Irradiation conditions and measured mechanical properties of six MWNTs.⁴⁰ Shown are the case number, gauge length, outer diameter, applied force at fracture, elongation, tensile strength^a and Young's modulus^a. Test 6 corresponds to the images shown in Fig. 1.16.

Test #	Gauge Length [μm]	Outer Dia. [nm]	Ion Radiation Dose [e cm^{-2}]	Electron Radiation Dose [e cm^{-2}]	Breaking Force [μN]	ΔL [nm]	σ_s^a [GPa]	E^a [GPa]
1	6.69	191	10^{14}	-	31.1	195.6	152.5	5,200
2	3.02	142	0.5×10^{14}	-	20.4	101.2	134.5	4,000
3	2.85	169	-	4.5×10^{14}	9.9	143.8	54.8	1,100
4	3.30	108	-	1.5×10^{14}	4.3	97.5	37.3	1,300
5	3.82	96	-	-	1.9	221.9	18.5	300
6	2.06	42	-	-	2.1	156.8	48.5	1,000

^aStress and strain are computed under the assumption that only the outermost shell of the MWNT bears the load (i.e. the cross-sectional area is taken to be that of the outermost shell alone).

using a 30 kV accelerating voltage. An in-situ TEM tensile test was then performed using the MEMS device. The corresponding inset of Fig. 1.17 shows clearly that the entire cross section broke as opposed to the typical telescoping, “sword-in-sheath” mechanism. Thus stress and modulus values reported in Tab. 1.1, which were computed assuming only the outermost shell to be load bearing, appear meaningless in this case. In fact, ion irradiated specimens exhibit values of Young's modulus of 5,200 and 4,000 GPa which are significantly higher than those reported elsewhere in the literature based on quantum mechanics calculations.^{53–55} Note also that Ding *et al.*¹³ reported moduli ranging from 620 to 1,200 GPa based on the assumption that only the outermost shell is load bearing. However, they do not provide evidence that only the outer shell failed.

MWNTs exposed to electron beam irradiation also showed greater stiffness than the unexposed sample, although to a lesser degree. In Test 4 (see Tab. 1.1), the MWNT was exposed to electron beam radiation with a flux of $1.5 \times 10^{19} \text{ e cm}^{-2}\text{s}^{-1}$ for 100 seconds within the TEM at an acceleration voltage of 200 kV. In this case, the failure was telescopic in nature as shown in the corresponding inset of Fig. 1.17. However, high-resolution TEM images show that more than one shell broke simultaneously rather than only the outermost shell. Thus again, the computed values of stress and strain based on the outermost shell assumption, do not accurately represent the true material behavior.

In summary, tensile tests of MWNTs exposed to high-energy electron or

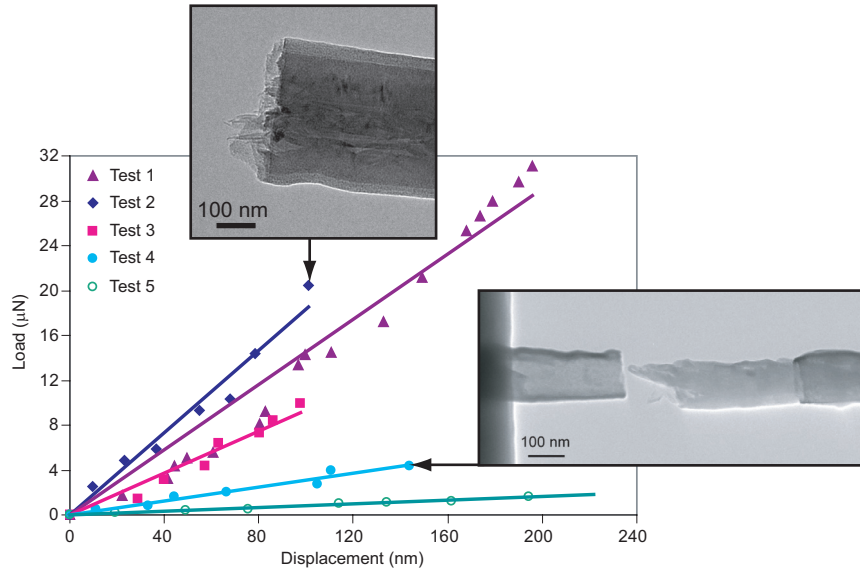


Fig. 1.17. Force-displacement data measured for multi-walled carbon nanotubes exposed to varying degrees and types of radiation. Corresponding irradiation conditions and test parameters are summarized in Tab. 1.1.

ion beam irradiation reveal changes in the mode of failure, suggesting that the irradiation introduces crosslinks between shells. Others have reported corroborating evidence based on experiments (for single-walled carbon nanotube bundles) and first principle calculations.^{56–58} Above a certain energy threshold, electron and ion beams can produce vacancies in the nanotube shells and corresponding interstitials in the inter-shell spacing.⁵⁶ Moreover, molecular dynamics simulations revealed that these interstitial atoms can form stable and covalent bonds between shells.⁵⁷ These simulations further demonstrated that the development of covalent bonds under moderate beam irradiation can increase the failure strength of MWNTs while excessive irradiation degrades the mechanical properties due to structural damage (cluster of vacancies) and/or amorphization.^{57,58} The experimental observations reported here agree strongly with the predictions of these simulations.

These findings show that both electron and ion irradiation could be used to enhance the mechanical properties of MWNTs. However, in light of the observed changes in failure mechanisms, conclusions based on existing stress and strain data computed under the assumption that only the

outermost shell bears the load should be drawn with caution. The observations reported here suggest there is some degree of load sharing between shells. For this reason, conclusions inferred from the data reported here focus on the stiffness of the nanostructures, which were measured directly. With advances in TEM image acquisition, the MEMS-based testing technique reported here should allow direct imaging of the the evolution of the failure and the number of shells failing simultaneously.

1.6. Summary

Mechanical characterization of nanometer-scale materials and structures presents a unique set of challenges. The excellent force and displacement resolution of MEMS make them ideal components for material characterization. This chapter presented the modeling and analysis involved in the design of a MEMS-based material testing system allowing simultaneous load-displacement measurement combined with real-time SEM or TEM imaging of the specimen. This system uses a thermal actuator to apply a tensile load and a differential capacitance displacement sensor of known stiffness to determine the applied load. An analytical model of the thermal actuator involved an electrothermal analysis to determine the temperature distribution in the actuator, followed by a thermomechanical analysis to determine the resulting displacement. A coupled-field finite element analysis confirms the analytical model. The differential capacitive load sensor was analyzed to determine the output voltage for a given displacement. A set of design criteria were established based on the analyses as guidelines for design of similar devices. Finally, examples of application of the MEMS-based material testing system to polysilicon thin films, palladium nanowires, and multi-walled carbon nanotubes were presented. Tensile tests of palladium nanowires demonstrated a major strength increase as compared to bulk palladium. Tensile tests of multi-walled carbon nanotubes exposed to varying degrees of electron and ion beam irradiation showed differences in failure mechanisms and an increase in stiffness with the level of irradiation. This is attributed to the formation of crosslinks between shells.

Acknowledgments The authors thank Alberto Corigliano for his valuable discussions and contributions in the analysis of the thermal actuator.

References

1. M. M. J. Treacy, T. W. Ebbesen, and J. M. Gibson, Exceptionally high young's modulus observed for individual carbon nanotubes, *Nature*. **381** (6584), 678–680, (1996).
2. P. Poncharal, Z. L. Wang, D. Ugarte, and W. A. de Heer, Electrostatic deflections and electromechanical resonances of carbon nanotubes, *Science*. **283**(5407), 1513–1516, (1999).
3. P. E. Marszalek, W. J. Greenleaf, H. Li, A. F. Oberhauser, and J. M. Fernandez. Afm captures quantized plastic deformation in gold nanowires. In ed. 97, *Proceedings of the National Academy of Sciences*, pp. 6282–6286, (2000).
4. W. C. Oliver and G. M. Pharr, An improved technique for determining hardness and elastic-modulus using load and displacement sensing indentation experiments, *Journal of Materials Research*. **7**, 1564, (1992).
5. M. T. A. Saif and N. C. MacDonald, A milli newton microloading device, *Sensors and Actuators A: Physical*. **52**, 65–75, (1996).
6. H. Kahn, R. Ballarini, R. L. Mullen, and A. H. Heuer. Electrostatically actuated failure of microfabricated polysilicon fracture mechanics specimens. In *Proceedings of the Royal Society of London A*, vol. 455, pp. 3807–3823, (1999).
7. E. Wong, P. Sheehan, and C. Lieber, Nanobeam mechanics: elasticity, strength, and toughness of nanorods and nanotubes, *Science*. **277**, 1971–1975, (1997).
8. D. A. Walters, L. M. Ericson, M. J. Casavant, J. Liu, D. T. Colbert, K. A. Smith, and R. E. Smalley, Elastic strain of freely suspended single-wall carbon nanotube ropes, *Applied Physics Letters*. **74**(25), 3803–3805, (1999).
9. J. P. Salvetat, G. A. D. Briggs, J. M. Bonard, R. R. Bacsa, A. J. Kulik, T. Stockli, N. A. Burnham, and L. Forro, Elastic and shear moduli of single-walled carbon nanotube ropes, *Physical Review Letters*. **82**(5), 944–947, (1999).
10. I. Chasiotis and W. G. Knauss, The mechanical strength of polysilicon films: 1. the influence of fabrication governed surface conditions, *Journal of the Mechanics and Physics of Solids*. **51**, 1533–1550, (2003).
11. W. N. Sharpe, K. M. Jackson, and K. J. Hemker, Effect of specimen size on young's modulus and fracture strength of polysilicon, *Journal of Microelectromechanical Systems*. **10**(3), 317–326, (2001).
12. M.-F. Yu, O. Lourie, M. J. Dyer, K. Moloni, T. F. Kelly, and R. S. Ruoff, Strength and breaking mechanism of multiwalled carbon nanotubes under tensile load, *Science*. **287**, 637, (2000).
13. W. Ding, L. Calabri, K. Kohlhaas, X. Chen, D. Dikin, and R. Ruoff, Modulus, fracture strength, and brittle vs. plastic response of the outer shell of arc-grown multi-walled carbon nanotubes, *Experimental Mechanics*. **online**, (2006).
14. Z. W. Pan, S. S. Xie, L. Lu, B. H. Chang, L. F. Sun, W. Y. Zhou, G. Wang, and D. L. Zhang, Tensile tests of ropes of very long aligned multiwall carbon nanotubes, *Applied Physics Letters*. **74**(21), 3152–3154, (1999).

15. A. Haque and M. T. A. Saif, Novel technique for tensile testing of submicron scale freestanding specimens in sem and tem, *Experimental Mechanics*. **42**, 123–128, (2002).
16. A. Haque and M. T. A. Saif, Deformation mechanisms in free-standing nano-scale thin films: A quantitative in-situ tem study, *Proceedings of the National Academy of Science*. **101**, 6335–6340, (2004).
17. R. C. Hugo, H. Kung, J. Weertman, R. Mitra, J. Knapp, and D. Follstaedt, In-situ tem tensile testing of dc magnetron sputtered and pulsed laser deposited ni thin films, *Acta Materialia*. **51**, 1937–1943, (2003).
18. M. Ke, S. A. Hackney, W. W. Milligan, and E. C. Aifantis, Observation and measurement of grain rotation and plastic strain in nanostructured metal thin films, *Nanostruct. Mater.* **5**(6), 689, (1995).
19. W. van Arsdell and S. Brown, Subcritical crack growth in silicon mems, *Journal of Microelectromechanical Systems*. **8**, 319–327, (1999).
20. H. Kahn, N. Tayebi, B. Ballerini, R. Mullen, and A. Heuer, Fracture toughness of polysilicon mems devices, *Sensors and Actuators A*. **82**, 274–280, (2000).
21. H. Kahn, B. Ballerini, and A. Heuer, On-chip testing of mechanical properties of mems devices, *MRS Bull.* **26**, 300–301, (2001).
22. L. Chu, L. Que, and Y. Gianchandani, Measurements of material properties using differential capacitive strain sensors., *Journal of Microelectromechanical Systems*. **11**, 489–98, (2002).
23. E. Fischer and P. Labossiere. In *Proceedings of the SEM Annual Conference on Exp. and App. Mechanics*, Milwaukee, WI, (2002).
24. Y. Zhu and H. D. Espinosa, An electromechanical material testing system for in situ electron microscopy and applications, *Proceedings of the National Academy of Sciences of the United States of America*. **102**(41), 14503–14508, (2005).
25. Y. Zhu, A. Corigliano, and H. D. Espinosa, A thermal actuator for nanoscale in situ microscopy testing: design and characterization, *Journal of Micromechanics and Microengineering*. **16**, 242–253, (2006).
26. Y. Zhu, N. Moldovan, and H. D. Espinosa, A microelectromechanical load sensor for in situ electron and x-ray microscopy tensile testing of nanostructures, *Applied Physics Letters*. **86**, (2005).
27. W. C. Tang, T. C. H. Nguyen, and R. T. Howe, Laterally driven polysilicon resonant microstructures, *Sensors and Actuators*. **20**(1-2), 25–32, (1989).
28. R. Legtenberg, A. W. Groeneveld, and M. Elwenspoek, Comb-drive actuators for large displacements, *Journal of Micromechanics and Microengineering*. **6** (3), 320–329, (1996).
29. A. A. Geisberger, N. Sarkar, M. Ellis, and G. D. Skidmore, Electrothermal properties and modeling of polysilicon microthermal actuators, *Journal of Microelectromechanical Systems*. **12**(4), 513–523, (2003).
30. J. S. Park, L. L. Chu, A. D. Oliver, and Y. B. Gianchandani, Bent-beam electrothermal actuators - part i: Single beam and cascaded devices, *Journal of Microelectromechanical Systems*. **10**(2), 247–254, (2001).
31. L. L. Chu and Y. B. Gianchandani, A micromachined 2d positioner with

- electrothermal actuation and sub-nanometer capacitive sensing, *Journal of Micromechanics and Microengineering*. **13**(2), 279–285, (2003).
32. M. F. Pai and N. C. Tien, Low voltage electrothermal vibromotor for silicon optical bench applications, *Sensors and Actuators A-Physical*. **83**(1-3), 237–243, (2000).
 33. H. Kapels, R. Aigner, and J. Binder, Fracture strength and fatigue of polysilicon determined by a novel thermal actuator, *IEEE Transactions on Electron Devices*. **47**(7), 1522–1528, (2000).
 34. M. Chiao and L. W. Lin, Self-buckling of micromachined beams under resistive heating, *Journal of Microelectromechanical Systems*. **9**(1), 146–151, (2000).
 35. C. D. Lott, T. W. Mclain, J. N. Harb, and L. L. Howell, Modeling the thermal behavior of a surface-micromachined linear-displacement thermomechanical microactuator, *Sensors and Actuators A-Physical*. **101**(1-2), 239–250, (2002).
 36. Q. A. Huang and N. K. S. Lee, Analytical modeling and optimization for a laterally-driven polysilicon thermal actuator, *Microsystem Technologies-Micro-and Nanosystems-Information Storage and Processing Systems*. **5**(3), 133–137, (1999).
 37. N. D. Mankame and G. K. Ananthasuresh, Comprehensive thermal modelling and characterization of an electro-thermal-compliant microactuator, *Journal of Micromechanics and Microengineering*. **11**(5), 452–462, (2001).
 38. L. Que, J. S. Park, and Y. B. Gianchandani, Bent-beam electrothermal actuators - part i: Single beam and cascaded devices, *Journal of Microelectromechanical Systems*. **10**(2), 247–254, (2001).
 39. Y. B. Gianchandani and K. Najafi, Bent-beam strain sensors, *Journal of Microelectromechanical Systems*. **5**(1), 52–58, (1996).
 40. H. D. Espinosa, Y. Zhu, and N. Moldovan, Design and operation of a mems-based material testing system for nanomechanical characterization, *To appear in Journal of Microelectromechanical Systems*. (2006).
 41. S. D. Senturia, *Microsystem design*. (Kluwer Academic Publishers, Boston, 2002).
 42. P. E. Boser. Electronics for micromachined inertial sensors. In *IEEE International Conference on Solid-State Sensors and Actuators*, Chicago (June, 1997).
 43. B. E. Boser and R. T. Howe, Surface micromachined accelerometers, *IEEE Journal of Solid-State Circuits*. **31**(3), 366–375, (1996).
 44. J. M. Huang, K. M. Liew, C. H. Wong, S. Rajendran, M. J. Tan, and A. Q. Liu, Mechanical design and optimization of capacitive micromachined switch, *Sensors and Actuators A-Physical*. **93**(3), 273–285, (2001).
 45. V. Del Toro, *Engineering circuits*. (Prentice Hall, Englewood Cliffs, NJ, 1986).
 46. A. Corigliano, B. De Masi, A. Frangi, C. Comi, A. Villa, and M. Marchi, Mechanical characterization of polysilicon through on chip tensile tests, *Journal of Microelectromechanical Systems*. **13**(2), 200–219, (2004).
 47. M. Ehmann, P. Ruther, M. von Arx, H. Baltes, and O. Paul, Operation and short-term drift of polysilicon-heated cmos microstructures at temperatures

- up to 1200 k, *Journal of Micromechanics and Microengineering*. **11**(4), 397–401, (2001).
48. I. Chasiotis and W. G. Knauss, The mechanical strength of polysilicon films: Part 1. the influence of fabrication governed surface conditions, *Journal of the Mechanics and Physics of Solids*. **51**(8), 1533–1550, (2003).
 49. T. H. Courtney, *Mechanical Behavior of Materials*. (McGraww-Hill, 2000).
 50. H. Espinosa, B. Prorok, and B. Peng, Plasticity size effects in freestanding submicron polycrystalline fcc films subjected to pure tension, *Journal of the Mechanics and Physics of Solids*. **52**, 667–689, (2004).
 51. M. Uchic, D. Dimiduk, J. Florando, and N. W., Sample dimensions influence strength and crystal plasticity, *Science*. **305**, 986–989, (2004).
 52. A. Barber, I. Kaplan-Ashiri, S. Cohen, R. Tenne, and H. Wagner, Stochastic strength of nanotubes: an appraisal of available data, *Composites Science and Technology*. **65**, 2830–2384, (2005).
 53. S. Zhang, S. Mielke, R. Khare, D. Troya, R. Ruoff, G. Schatz, and T. Belytschko, Mechanics of defects in carbon nanotubes: Atomistic and multiscale simulations, *Physical Review B*. **71**, 115403, (2005).
 54. S. Mielke, D. Troya, S. Zhang, J. Li, S. Xiao, R. Car, R. Ruoff, G. Schatz, and T. Belutschko, The role of vacancy defects and holes in the fracture of carbon nanotubes, *Chemical Physics Letters*. **390**, 413–420, (2004).
 55. D. Troya, S. Mielke, and G. Schatz, Carbon nanotube fracture-differences between quantum mechanical mechanisms and those of empirical potentials, *Chemical Physics Letters*. **382**, 133–141, (2003).
 56. W. Smith and D. Luzzi, Electron irradiation effects in single wall carbon nanotubes, *Journal of Applied Physics*. **90**, 3509–3515, (2001).
 57. M. Huhtala, A. Krasheninnikov, J. Aittoniemi, S. Stuart, K. Nordlund, and K. Kaski, Improved mechanical load transfer between shells of multiwalled carbon nanotubes, *Physical Review B*. **79**, 045404, (2004).
 58. J. Pomoell, A. Krasheninnikov, K. Nordlund, and J. Keinonen, Ion ranges and irradiation-induced defects in multiwalled carbon nanotubes, *Journal of Applied Physics*. **96**(5), 2864–2871, (2004).

Index

- actuators
 - comb drive, 5
 - electrothermal, 5, 7
 - buckling, 17
 - finite element analysis, 15
 - modeling, 7
- load sensor
 - differential capacitive, 19
- material testing, 25
 - carbon nanotubes, 28
 - nanowires, 26, 27
 - thin films, 26, 27
- MEMS, 5
 - equivalent circuit, 21
 - lumped model, 14